Spherical harmonic decomposition of gravitational waves across mesh refinement boundaries

David R. Fiske*
Department of Physics, University of Maryland, College Park, Maryland 20742-4111 and
Exploration of the Universe Division, NASA Goddard Space Flight Center, Greenbelt, Maryland 20771

John Baker, James R. van Meter, and Joan M. Centrella
Exploration of the Universe Division, NASA Goddard Space Flight Center, Greenbelt, Maryland 20771

We evolve a linearized (Teukolsky) solution of the Einstein equations with a non-linear Einstein solver. Using this testbed, we are able to show that such gravitational waves, defined by the Weyl scalars in the Newman-Penrose formalism, propagate faithfully across mesh refinement boundaries, and use, for the first time to our knowledge, a novel algorithm due to Misner to compute spherical harmonic components of our waveforms. We show that the algorithm performs extremely well, even when the extraction sphere intersects refinement boundaries.

I. INTRODUCTION

Computing candidate waveforms for gravitational wave observatories remains one of the premiere goals of numerical relativity. In order to achieve this goal, one needs to sensibly define radiation, develop numerical codes and algorithms to solve the non-linear Einstein equations, and handle a variety of technical problems such as modeling singular black hole spacetimes and allocating available computer resources in problems with multiple dynamical length scales.

In this brief report, we define a simplified problem in which to study the propagation of gravitational waves and to study a candidate algorithm due to Misner [1] for compute the spherical harmonic components of radiation fields. Consistent with our recent efforts to introduce mesh refinement techniques into numerical relativity, to help deal with the problem of efficiently allocating computer resources in problems with multiple dynamical length scales, we use this test problem to study how faithfully gravitational waves propagate across mesh refinement boundaries, and to validate the Misner algorithm in the case where the spheres on which the spherical harmonics are computed cross through refinement boundaries.

We are motivated to consider the case where extraction spheres cross refinement boundaries in part because in our particular fixed mesh refinement scheme (provided by the `PARAMESH` package [2]) we find that there are frequently few or no radii for extraction spheres inside single mesh refinement regions when we place refinement boundaries at locations that most efficiently use available computer memory. More importantly, however, we look forward to using *adaptive* mesh refinement, in which we anticipate having refinement boundaries dynamically pass through extraction regions as high resolution grids track wavefronts. In this case, it will be essential that our spherical harmonic decomposition algorithm work in the presence of refinement boundaries.

Finally, we note that setting down in detail a simple but useful test case can play an important role in making comparisons between different codes and different algorithms, much in the spirit of Ref. [3]. This is especially useful for the spherical harmonic problem since, at this point, few if any other numerical relativity groups have begun implementing this technology. We hope that this work can serve as a benchmark for future efforts.

II. METHODOLOGY

Computing gravitational waves from numerical simulations of the Einstein equations requires combining a variety of nearly mathematical formalisms and numerical techniques into a single code. In Section II A, we briefly discuss our particular Einstein solver. We are deliberately brief on this point because, for our present purposes, we find it useful to abstract away from the details of how the simulation is done, and consider the problem of analyzing data once we have it. The methods that we present, implement, and test here are not specific to any particular formalism or to our code. These more general issues are made explicit in the rest of the section where we define gravitational radiation via the Weyl scalars in the Newman-Penrose formalism in Section II B, and discuss the need and a method for computing spherical harmonic components of radiation data in Section II C.

A. The Hahndol Code

Our code is a fully three-dimensional, non-linear Einstein solver. We use a fairly standard formulation of the 3+1 Einstein evolution equations known as BSSN [4, 5]; our particular implementation was described in detail in Ref. [6]. Because the formulation of the equations is not of primary interest here, and because the basics of the

*Current Address: Decisive Analytics Corporation, 1235 South Clark Street, Arlington, VA 22202

BSSN system are widely know, we do not focus on these equations.

The code uses second-order accurate finite differencing to approximate spatial derivatives and the iterative Crank-Nicholson method [7] to integrate the evolution equations forward in time. In both our previous and current work, we have verified second order convergence in our results.

Our code parallel code uses the PARAMESH libraries [2] to handle domain decomposition and inter-processor synchronization. In addition, these libraries enable us to use non-uniform grids to focus computational resources in specific areas of the computational domain. Although the libraries support, and we look forward to using, the ability to adaptively modify the grid structure during the course of a simulation (adaptive mesh refinement), we currently fix our grid structures in advance using a priori estimates of where to focus resolution (fixed mesh refinement).

Previous studies, showed that the Hahndol code is able to propagate strong gravitational waves (defined in terms of metric components) across mesh refinement boundaries [8], and that the same code can handle strong, dynamical potentials moving between refinement regions [6]. In this paper we again focus on wave propagation, this time using a more formal definition of graviational radiation, the Weyl scalars in the Newman-Penrose formalism, and on analyzing such data in a meaningful way.

B. Weyl Scalars

We use the Newman-Penrose formalism to compute gravitational radiation quantities. In this formalism, one chooses a tetrad of four null basis vectors. These vectors are conventionally labled l^a, n^a, m^a, and $\bar{m}^a$.[1] Of these, l^a and n^a are real and point along "outgoing" and "ingoing" directions, respectively. The vectors m^a and $\bar{m}^a$ span "angular" directions and are complex conjugates of each other. These vectors are always chosen to satisfy the orthogonality conditions

$$l^a m_a = n^a m_a = 0. \tag{1}$$

In addition, we impose the normalization conditions $l^a n_a = -1$ and $m^a \bar{m}_a = +1$, which are imposed by most, but not all, authors (cf. Ref. [9]).

Given a tetrad, tensor quantities can be recast as sets of coordinate scalars by projecting tensor components onto the basis. Applying this procedure to the Weyl tensor C_{pqrs} yields five complex scalars. This is particularly useful for gravitational wave studies since one of the five,

$$\Psi_4 = -C_{pqrs} n^p \bar{m}^q n^r \bar{m}^s, \tag{2}$$

represents outgoing graviational waves. Indeed, the primary goals of this paper are to construct Ψ_4 in some sample, numerically evolved spactimes, and to demonstrate that such computations are accurate characterizations of the wave content of the spacetime.

In vacuum, which is the only case that we consider here, the Weyl tensor is numerically equal to the Riemann tensor.

As a technical point, it is important to note that, although our code uses a 3+1 decomposition of the Einstein equations, Eq. 2 is written in terms of four dimensional, spacetime quantities. Since, in code, we have only 3+1 quantities on a single time slice from which to compute the four dimensional Riemann tensor, we follow Ref. [10] and write

$$^{(4)}R_{ijkl} = R_{ijkl} + 2K_{i[k}K_{l]j} \tag{3a}$$

$$^{(4)}R_{0jkl} = -2\left(K_{j[k,l]} + \Gamma^p_{j[k}K_{l]p}\right) \tag{3b}$$

$$^{(4)}R_{0j0l} = R_{jl} - K_{jp}K^p_{\ l} + KK_{jl} \tag{3c}$$

which express four dimension quantites on the left hand sides in terms of 3+1 quantities on the right.[2] Here K_{ij} is the extrinsic curvature tensor for a spatial slice as imbedded in the full spacetime manifold, and K is its trace. The symbols Γ^p_{jk}, R_{ijkl}, and R_{jl} stand for, respecitively, the connection coefficients, Riemann tensor, and Ricci tensor associated with the three dimensional spatial metric on the slice.

C. Spherical harmonic decomposition

In our simulations, we would like to be able to extract the spherical harmonic components of gravitational waves. We find this very valuable when analyzing the data because

1. Numerical noise tends to have higher angular frequency than genuine wave signals, and is therefore filtered by the decomposition process.

2. A priori knowledge about symmetries in the data or dominant modes associate with physical processes allow important checks on the plausibility of numerical solutions (especially when exact solutions are not available).

---

[1] Note that, although our code uses a 3+1 decomposition of the Einstein equations, indices on Newman-Penrose quantities are always understood to run over four dimensional spacetime indices.

[2] There are two errors in Ref. [10] associated with what we call Eq. 3. First there is a factor of two difference between Eq. 3b, which is correct, and the corresponding equation in Ref. [10]. Second, Eq. 3 in this paper properly reflects the fact that the left hand sides refer to the four dimensional Riemann tensor.

3. Analysis of spherical harmonic components will be important in quantifying the amount of energy and momentum carried by gravitational radiation.

In practice, however, we face a technical problem in computing spherical harmonic components of our data. While our data is stored on a cubic grid, the spherical harmonic components

$$ {}_s\Phi_{lm}(t,r) = \oint {}_s\bar{Y}_{lm}(\theta,\phi)\Phi(t,r,\theta,\phi)d\Omega \qquad (4) $$

of a general (complex valued) function Φ in a spherical harmonic basis with spin-weight s are defined by an integral over a sphere. Computing the integral in Eq. 4 requires some type of interpolation from grid points to points on the sphere of radius r.

One could solve this problem by the straightforward method of (1) interpolating the grid function Φ to points on the sphere, and then (2) using some numerical approximation to the integral in Eq. 4. This process of iterpolation followed by integration would then need to be performed at each time, at each radius, and for every function for which the spherical harmonic components are desired.

We adopt a different algorithm due to Misner. Following Ref. [1], we smear the surface integral in Eq. 4 into a volume integral over a shell of half-thickness Δ, and create an orthonormal basis for functions on this shell by combining the spherical harmonics in the angular directions with the first N Legendre polynomials in the radial direction. This approach, which we describe in more detail in Appendix A, has the advantage that, given the parameters Δ and N, one needs only compute a relatively small number of weights for computing the volume integral, and that these weight depend only on the grid structure and the radius of extraction. This means that the weights can be computed once at the beginning of a simulation and stored. Further interpolations are not need, and the weights are valid for all functions.

The question of how to choose the input parameters Δ and N was addressed in Refs. [11, 12]. Under the assumption (motivated by the analysis in the references) that Δ is chosen proportional to the grid spacing, the parameter N controls the order of convergence of the decomposition algorithm, while the parameter Δ controls the size of the error at that order. This analysis leads to the

> **Rule of Thumb**: Choose N just large enough to ensure that the error term proportional to Δ is not of leading order in grid spacing. Choose Δ just large enough to safely resolve P_N on the shell.

For second order accurate codes, like ours, with grid spacing h, Refs. [11, 12] suggest choosing $N = 2$ and $\Delta = 3h/4$ based on this rule and emprical experiments. In cases where the shell passes through multiple refinement regions, the grid spacing of the *coarsest* grid through which the shell passes should be chosen to ensure that P_N is resolved on both sides of the interface. We follow these suggestions for all work presented here.

III. TEUKOLSKY WAVES

We apply our techniques to two sample problems. The first is a linearized solution to the Einstein equations due to Teukolsky [13]. We choose the Teukolsky wave as our first test problem because (1) it has an exact solution, so we can compute our numerical errors exactly, (2) it is linear, so we can extract our waves at small radii. The second point saves time and resources in the early stages of testing. Waiting for waves generated by non-linear sources to propage to the wave zone is costly, and couples problems with evolving the sources to problems with extracting the waves.

We tackle a non-linear problem in our second test case, a head-on collision of equal mass black holes, in Section IV.

A. Analytic Preliminaries

Our first problem studies a Teukolsky wave spacetime [13]. This is a solution to the linearized Einstein equations, which represents a weak gravitational wave propagating through space. The linear nature of the initial data, makes this an excellent first test problem for two reasons. First, the there is an analytic solution for all times, allowing an exact calculation of numerical errors for convergence and accuracy studies. Second, because the wave is linear in the initial data, we are able to extract our waveforms at small radii and short evolution times. This second fact is extremely useful for debugging algorithms, and also allows higher resolutions for a fixed problem size since the boundaries of the computational domain need not be as large as it would in problems (like the head-on collision described in Section IV) in which the waves are generated by non-linear sources and must propagate to the wave zone before being extracted.

Although the Teukolsky solution is well-known, we summarize it here for completeness and to establish notation. We use the pure $l = 2$, $m = 0$ (in a spin-weight -2 basis) solution.

The spacetime metric, given in full in Appendix B, is written in terms of functions

$$ A = 3\left(\frac{F^{(2)}}{r^3} + \frac{3F^{(1)}}{r^4} + \frac{3F}{r^5}\right) \qquad (5a) $$

$$ B = -\left(\frac{F^{(3)}}{r^2} + \frac{3F^{(2)}}{r^3} + \frac{6F^{(1)}}{r^4} + \frac{6F}{r^5}\right) \qquad (5b) $$

$$ C = \frac{1}{4}\left(\frac{F^{(4)}}{r} + \frac{2F^{(3)}}{r^2} + \frac{9F^{(2)}}{r^3} + \frac{21F^{(1)}}{r^4} + \frac{21F}{r^5}\right) \qquad (5c) $$

and in terms of a free generating function $F = F(t-r)$.

The notation

$$F^{(n)} = \left[\frac{d^n F(x)}{dx^n}\right]_{x=t-r} \tag{6}$$

denotes various derivatives. Taking F as a function of $t-r$ corresponds to outgoing waves. To generate an ingoing solution, change the argument of F to $t+r$, and change, in Eq. 5, the sign in front of all of the terms with *odd* numbers of derivatives.[3]

Furthermore, we follow Choi et al. [8] in choosing

$$F(x) = \frac{\mathcal{A}x}{\lambda^2} e^{-x^2/\lambda^2} \tag{7}$$

as the exact form of the generating function, where the free parameters $\mathcal{A}$ and λ represent the amplitude and the width of the wave respectively. The natural length unit in the problem is λ, and we consistently choose $\mathcal{A} = 2 \times 10^{-6}\lambda$. Moreover we take an equal superposition of an ingoing wave and an outgoing wave, both centered at the origin, for the initial data. This particular choice has a moment of time symmetry that allows us to set the extrinsic curvature tensor to zero.

Choosing F of the form in Eq. 7 gives a waveform with oscillations but of essentially compact support. This is ideal for testing codes with boundaries because it makes clear when the wave passes through those boundaries, and allows one to easily detect any reflections that occur due to poor interface conditions.

For our 3+1 code, we use this analytic solution to generate the intial data, and evolve forward in time using the gauge conditions lapse $\alpha = 1$ and shift $\beta^i = 0$.

In this work, we use the Kinnersley tetrad [14]

$$l = \frac{1}{\Delta}(r^2 + a^2, \Delta, 0, a) \tag{8a}$$

$$n = \frac{1}{2\Sigma}(r^2 + a^2, -\Delta, 0, a) \tag{8b}$$

$$m = \frac{1}{\sqrt{2}(r + ia\cos\theta)}(ia\sin\theta, 0, 1, i\csc\theta) \tag{8c}$$

for the linear wave problem.[4] Eqs. 8 give the tetrad in terms of the Boyer-Lindquist coordinates for a Kerr black hole. In these equations, $\Delta = r^2 - 2Mr + a^2$, $\Sigma = r^2 + a^2\cos^2\theta$, M is the mass of the Kerr black hole, and a is its spin. Because Boyer-Lindquist coordinates are compatible with the coordinate system used for the Teukolsky metric (Eq. B1) when $M = a = 0$, we find this coordinate expression for the tetrad completely acceptable for this problem.

[3] Note that Ref. [8] improperly describes the construction of ingoing waves. The description here, which matches the original reference, Ref. [13], is correct.

[4] The first component of m^a should have the $\sin\theta$ term in the numerator as in Eq. 8c; the corresponding equation in Ref. [10] is incorrect.

For this relatively simple spacetime, one can compute the value of the Newman-Penrose quantity

$$\Psi_4 = \frac{\sin^2\theta}{16}\left[-12\frac{\partial^2 C}{\partial t^2} + 6\frac{\partial^2 A}{\partial t^2} + r\left(3\frac{\partial^3 B}{\partial t^3} + \frac{\partial^3 A}{\partial t^3}\right)\right] \tag{9}$$

which represents outgoing gravitational radiation. Noting that

$${}_{-2}Y_{20}(\theta,\phi) = \sqrt{\frac{15}{32\pi}}\sin^2\theta \tag{10a}$$

$$= \sqrt{\frac{5}{6}}\left(Y_{00}(\theta,\phi) - \frac{1}{\sqrt{5}}Y_{20}(\theta,\phi)\right) \tag{10b}$$

it is clear that, as claimed, Eq. 9 is a pure $l = 2$, $m = 0$ mode. Note also that Eq. 10b provides a way to compute a spin-weight -2 spherical harmonic component from the usual (spin-weight 0) spherical harmonic components. This is essential for us because, although we would like spin-weight -2 results, our current implementation of the Misner algorithm computes only spin-weight 0 components.

B. Numerical Results

We evolved initial data specified by the Teukolsky solution described in Section III A on a domain with outer boundaries at 32λ and with a "box-in-box" refinement scheme. The boundaries were at 2λ, 4λ, 8λ, and 16λ; neighboring regions differed in resolution by a factor of two, with the finest regions surrounded by coarser regions. In order to compute convergence factors, we ran the code at innermost resolutions $\lambda/12$, $\lambda/24$, and $\lambda/48$.

We then attempted to compute the spherical harmonic components of that wave at five distinct "detectors" located at $r = 3\lambda$, 4λ, 5λ, 6λ, and 7λ. To help visualize how the refinement boundaries and the extraction radii are related geometrically, we find it useful to draw *extraction maps*, as shown in Fig. 1. The extraction maps make it clear that the shells used to compute the spherical harmonic components generically pass through multiple refinement regions, especially since in three dimensions the corners of the cubic refinement regions tend to pass through the spherical extraction shells. The extraction maps shown in Fig. 1 correspond to the innermost ($r = 3\lambda$) extraction radius in the coarsest run, and the $r = 6\lambda$ extraction radius in the medium resolution run. (Extraction maps for nearly all extraction radii and two resolutions appear in Ref. [11].) Note that only the innermost refinement regions are shown in the maps. In each case, the entire map was surrounded by additional (coarser) refinement regions.

Since we know the analytic solution for this test problem, we are able to make a detailed convergence study with three resolution levels. We were able to verify that not only the waveforms themselves, the extracted spherical harmonic components converge at second order

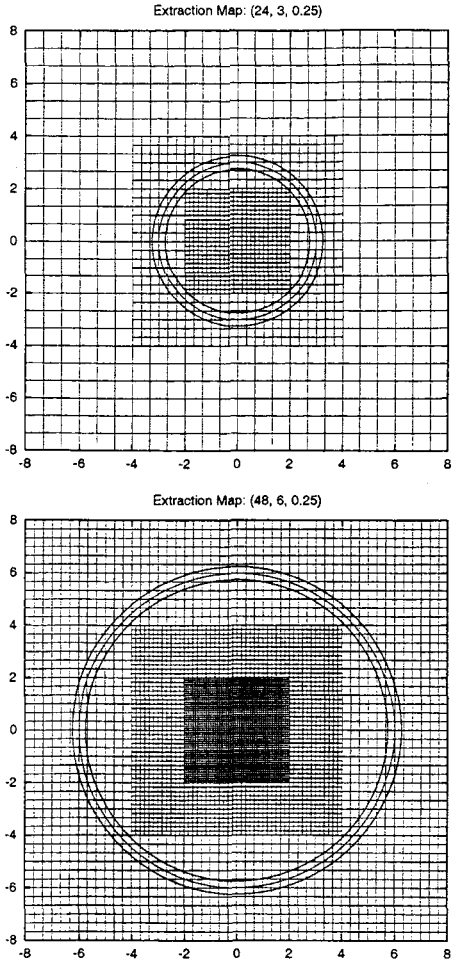

FIG. 1: Selected extraction maps. Each map is labeled with a triple of numbers (N, R, Δ), which indicate the number of (cell-centered) grid points across one coordinate direction in the coarsest region, the extraction radius (in units of λ), and the half-thickness of the shell. Note that the shells generically pass through multiple refinement regions, especially since, in three dimensions, the corners of the cubic refinement regions tend to poke through the spherical extraction shells. The three circles drawn on each graph show the extraction sphere and the edges of the finite-thickness shell around the sphere used in the Misner algorithm.

(as predicted), even with the extraction spheres passing through the refinement boundaries, and that the solution is highly accurate. We also find that the results are extremely consistent between the various extraction radii. Note in particular Fig. 2, which shows, in Panel A, a single wave as computed at distinct radii. The amplitude, to leading order, scales like $1/r$ and maintains its shape as it moves outward, consistent with the analytic solution. This is seen more clearly in Panel B in which the waveforms have been scaled-up by r and shifted to a single extraction radius. Up to higher order terms in $1/r$, these waveforms should match. As seen in the figure, the agreement is excellent.

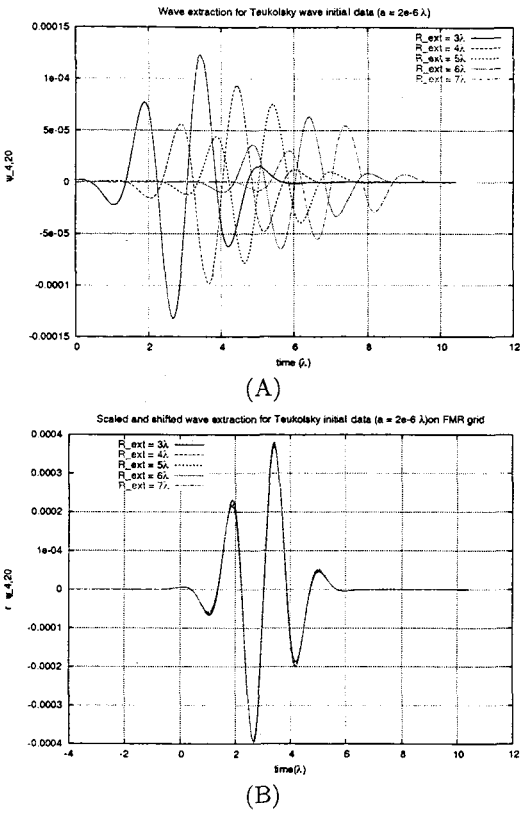

FIG. 2: The $l = 2$, $m = 0$ component of the Teukolsky wave, as computed at five different radii (highest resolution). The wave form is preserved up to the leading order $1/r$ scaling. Panel A shows the raw data. Panel B shows the same data, scaled-up by r and shifted in time to $t = 3\lambda$.

In evaluating the effects of the refinement boundaries on the spherical harmonic decomposition algorithm, one should bear in mind that no two of the extraction radii have the same geometric relationship with the refinement boundaries (cf. Fig. 1), and yet they nonetheless generate perfectly consistent results.

IV. BLACK HOLE HEAD-ON COLLISION

We also tested our techniques on a non-linear problem, which is more closely related to the astrophysical problems of interest to us. Our specific choice of the equal-mass head-on collision of two black holes tests our techniques on a fully non-linear problem, but also, consistent with our goal of testing our techniques, allows a variety of symmetries that we can use as checks on our numerical solutions.

A. Analytic Preliminaries

In our head-on collisions, we place two black holes, each of mass M, on the z axis at a coordinate distance of

$1.1515M$ from the origin. The initial data is generated by the puncture prescription of Ref. [15], which is a generalization of Brill-Lindquist initial data [16]. We then use the excision algorithm of Ref. [17] to avoid evolving the portions of our grid interior to the (seperate) event horizons of our initial data. We neither allow our excision regions to move nor switch to a single, larger excision region after a common horizon forms. Although one or both of these techniques will likely be desirable in future simulations, we find the simple approach sufficient to extract convergent waveforms.

Once we generate our initial data, we evolve it in our 3+1 code using the 1+log evolution equation

$$\frac{\partial \alpha}{\partial t} = -2\alpha K \tag{11}$$

for the lapse α, and the hyberbolic Gamma-driver evolution equations

$$\frac{\partial \beta^i}{\partial t} = \frac{3}{4}\alpha \psi_{BL}^{-4} B^i \tag{12a}$$

$$\frac{\partial B^i}{\partial t} = \frac{\partial \tilde{\Gamma}^i}{\partial t} - \eta B^i \tag{12b}$$

for the shift β^i. In these equations, K is the trace of the extrinsic curvature tensor for our slice, $\tilde{\Gamma}^i$ is the conformal connection function of the BSSN evolution system (cf. Ref. [5]), and B^i is defined by Eq. 12a to keep the gauge evolution equations first order in time. The quantity

$$\psi_{BL}(r) = \sum_{i=1}^{N} \left(1 + \frac{M_i}{2|\vec{r} - \vec{r}_i|}\right) \tag{13}$$

is the Brill-Lindquist factor used to generate puncture initial data for N black holes with masses M_i and positions $\vec{r}_i$. (In our case, $N = 2$ and $M_1 = M_2 = M$.) In our work, we choose the dissipation parameter $\eta = 2.8/M$, and set, at the initial time, $\alpha = 1$ and $\beta^i = 0$. These gauge conditions were first studied in Ref. [18].

For the head-on collision, we do not use the Kinnersley tetrad. We have no way of knowing for the head-on collision that the coordinate expressions in Eq. 8 are appropriate to our numerically evolved spacetime. (Indeed, for a general problem, one would assume that they are not appropriate.) For the head-on collision, we instead construct an orthonormalized tetrad from the numerically evolved spacetime using a Gramm-Schmidt procedure as described in Ref. [10].[5]

[5] We use the Teukolsky wave as a check on our implementation of the Gramm-Schmidt construction. In the limit of perturbed flatspace, the Gramm-Schmidt procedure recovers the Kinnersley tetrad up to a trivial rescaling of l^a and n^a. Comparisions of waveforms extracted from Teukolsky wave spacetimes with the two choices of tetrad match very closely when this rescaling is taken into account.

In the head-on case, we do not have an analytic solution for the Weyl scalars, so we can not directly compute the error in our solution. The symmetries of the problem, however, provide us with several analytic checks on our numerical results. Before discussion these symmetries specifically, however, it is worth making explicit a related point: there are three independent symmetry axes in this problem. The first is the symmetry of the physical problem, i.e. the axis along which the two black holes collide. The second is axis with respect to which the tetrad is computed. (Note, for example, the Kinnersley tetrad defined by Eq. 8, in which the existence of a prefered axis is manifest in the coordinate expressions.) The third is the axis with respect to which we compute the spherical harmonics. Only if we align all of these axes of symmetry (conventionally along the z axis) will all of our symmetry checks be true.[6]

Assuming that, as in the problem described here, all three symmetry axes are aligned, the numerical solution should have the following properties:

- $\mathrm{Re}\{\Psi_4\}$ is axially symmetric and is symmetric under the transformation $z \to -z$ up to the round-off level.
- $\mathrm{Im}\{\Psi_4\}$ converges to zero.
- Viewed in a spin-weight -2 basis, the dominent contribution to $\mathrm{Re}\{\Psi_4\}$ comes from the $l = 2$, $m = 0$ mode.
- Viewed in a spin-weight 0 basis, trunctation level errors in $\mathrm{Im}\{\Psi_4\}$ appear in only in modes with *odd* values of $l \geq 5$ and *even* values of m.

B. Numerical Results

For the head-on collision simulations, we again use a box-in-box mesh refinement scheme. We place our outer boundary at coordinate distance $128M$, and place refinement boundaries at $4M$, $8M$, $16M$, $32M$, and $64M$ (six levels total). We evole only one octant of our spacetime, using appropriate symmetry boundary conditions to mimic a full grid. Because of the octant symmetry conditions used, only one of the black holes appears in our evolved numerical grid. (The other is accounted for by the symmetry boundary conditions.) We ran simulations at three resolutions with interior resolutions of $M/16$, $M/24$, and $M/32$ in order to perform convergence tests.

[6] In addition, because, for example, the inner product $\oint {}_{-2}\bar{Y}_{22}(\theta,\phi)_0 Y_{l2}(\theta,\phi) d\Omega \neq 0$ for all $l \geq 2$, it is impossible to convert between the spin-weight -2 and spin-weight 0 bases in problems lacking axial symmetry, unless one computes spherical harmonic components at all values of l in the spin-weight 0 basis.

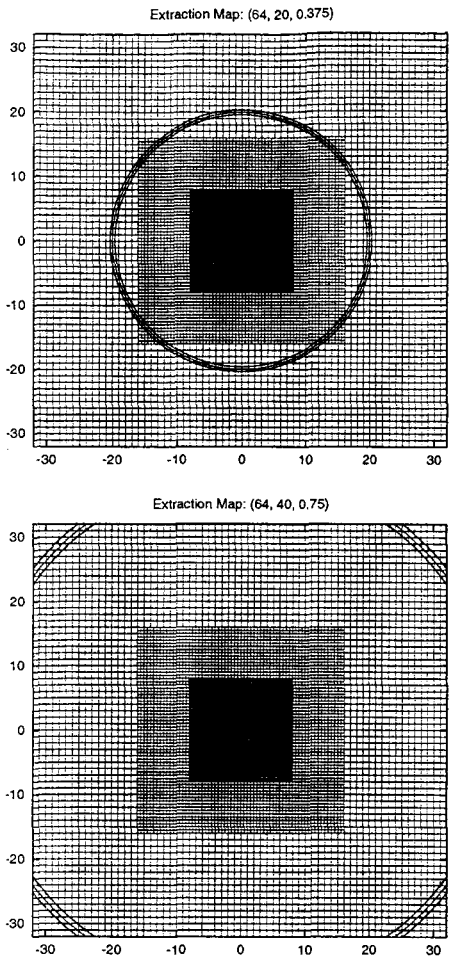

FIG. 3: Selected extraction maps for the head-on collsion. The maps accurately show the relative sizes and positions of refinement regions and the extraction shells used by the Misner algorithm for extractions at $r = 20M$ and $r = 40M$ in our lowest resolution simulation.

We excise a cubic region, centered on the puncture. The cube has sides of length $0.23125M$ The size shape, and location of the excision region remain fixed during the course of the run.

In these simulations, we extract our waveforms at $r = 20M$, $30M$, $40M$, and $50M$. Extraction maps for the $20M$ and $40M$ extractions in Fig. 3. Since this is a non-linear problem, we are forced to extract a larger radii than in the Teukolsky wave simulations in order to ensure that we are extracting in the wave zone.

With our data from the three resolutions, we were able to evaluate the convergence behavior of our waveform. Fig. 4 shows a three-point convergence plot for the $l = 2$, $m = 0$ (spin-weight -2) component of Ψ_4 extracted from our simulations. In the three point convergence graphs, we show $(\Psi_4^{(\mathtt{High})} - \Psi_4^{(\mathtt{Med})})$ and $4(\Psi_4^{(\mathtt{Med})} - \Psi_4^{(\mathtt{Low})})/9$, which should coincide, up to the effect of higher order error terms, for our second order accurate code, and our choice of relative grid spacings. The agreement is impressive.

Convergence plot of $\Psi_{4,20}$ for head-on collision goes here.

FIG. 4: A convegence plot of the $l = 2$, $m = 0$ (spin-weight -2) component of Ψ_4 for the equal mass black hole head-on collision problem.

Scaled and shifted waveforms for the head-on collision.

FIG. 5: A comparision between the $l = 2$, $m = 0$ components of Ψ_4 as computed at distinct radii. The waveforms have been scaled-up by r and shifted to the intermost extraction radius, $r = 20M$. Up to sub-leading terms in $1/r$, these scaled and shifted waveforms should coincide.

As with the Teukolsky wave, we should also be able to demonstrate agreement betwee the waveforms extracted at distinct radii, and indeed our numerical results are consistent with this expectation. Fig. 5 shows the $l = 2$, $m = 0$ component of Ψ_4 as extracted at four radii. As in Panel B of Fig. 2, the components have by scaled-up by r and shifted to the innermost extraction location for direct comparision. Up to sub-leading terms in $1/r$, waveforms scaled and shifted in this way should coincide, as they do in the figure.

V. DISCUSSION

We have presented a useful test problem for studying the propagation of gravitational wave through mesh refinement boundaries. We find, consistent with earlier results, that our interface conditions faithfully propagate gravitational waves. More importantly, we show for the first time that the Misner algorithm for computing spherical harmonic components on a cubic grid is viable in live simulations and validate in an application the numerical analysis performed on this algorithm in earlier work. Our results show that the algorithm works in the presence of mesh refinement boundaries even when the extraction spheres pass through those boundaries.

Because mesh refinement regions tend to be cubes, we find in our current simulations that this last point in crucial. There is frequently little or no room to locate finite-thickness shells such that they remain entirely in a single resolution region when we use box-in-box fixed mesh refinement. Moreover, we expect that, in the future, when we run simulations with *adaptive* mesh refinement, that high resolution regions will track wave fronts. In that case it would be almost inevitable that refinement boundaries would dynamically pass through the extraction region.

These results pave the way for further studies of the propagation of waves through mesh refinement boundaries and for applying the Misner algorithm in more astrophysically interesting situation in which the waves are generated by simulated, dynamical sources. We hope also that the simple test problem that we have presented here

can serve as a standard testbed for comparing such techniques in the future.

Acknowledgments

We would like to thank Charles Misner for providing advice as we implemented his algorithm. We also thank Breno Imbiriba, who has contributed to the recent development of the Hahndol code. This work was supported in part by NASA Space Sciences grant ATP02-0043-0056.

APPENDIX A: SUMMARY OF THE MISNER METHOD

This appendix provides a more detailed look at the Misner algorithm for computing spherical harmonic components of a function represented on a cubic grid. Additional details can be found in Misner's original paper, Ref. [1]. A detailed discussion of the trunction error as a function of the algorithm's parameters can be found in Refs. [11, 12].

Recall that the problem is to compute the spherical harmonic components Φ_{lm}, defined by Eq. 4, of a function Φ that is known only on vertices of a cubic lattice. (In this appendix, we suppress the spin-weight index s.) In order to begin, two definitions are need. First define a family of radial functions

$$R_n(r;R,\Delta) = r^{-1}\sqrt{\frac{2n+1}{2\Delta}}P_n\left(\frac{r-R}{\Delta}\right) \tag{A1}$$

in terms of the usual Legendre polynomials P_n. Here R and Δ are parameters that will be associated with the radius at which the spherical harmonic decomposition is desired and half of the thickness of a shell centered on that radius. From this, define

$$Y_{nlm}(r,\theta,\phi) = R_n(r)Y_{lm}(\theta,\phi) \tag{A2}$$

which form a complete, orthonormal set with respect to the inner product

$$\langle f|g\rangle = \int_S \bar{f}(x)g(x)d^3x \tag{A3}$$

on the shell $S = \{(r,\theta,\phi) \mid r \in [R-\Delta, R+\Delta]\}$. Note also that, because the functions R_n form a complete set in the radial direction,

$$\Phi_{lm}(t,R) = \int \rho(r;R,\Delta)\bar{Y}_{lm}(\theta,\phi)\Phi(r,\theta,\phi)d^3x \tag{A4}$$

with

$$\rho(r;R,\Delta) = \sum_{n=0}^{\infty} R_n(R;R,\Delta)R_n(r;R,\Delta), \tag{A5}$$

and that

$$\rho(r;R,\Delta) = r^{-2}\delta(R-r) \tag{A6}$$

is a delta function. (Compare Eq. A4 to Eq. 4.)

On a finite grid Γ, the inner product Eq. A3 will have the form

$$\langle f|g\rangle = \sum_{x\in\Gamma} \bar{f}(x)g(x)w_x \tag{A7}$$

where each point has some weight w_x. This weight was given the form

$$w_x = \begin{cases} 0 & |r-R| > \Delta + h/2 \\ h^3 & |r-R| < \Delta - h/2 \\ (\Delta + h/2 - |R-r|)h^2 & \text{otherwise} \end{cases} \tag{A8}$$

by Misner, where h is the grid spacing. Only cases with $\Delta > h/2$ are considered. This means, roughly, that points entirely within the shell S are weighted by their finite volume on the numerical grid, points entirely outside of the shell S have zero weight, and points near the boundary are weighted according to the fraction of their volume inside S.

With the numerical inner product Eq. A7, and letting capital Roman letters $A = (nlm)$ represent index groups, the Y_A are no longer orthonormal. Their inner product

$$\langle Y_A|Y_B\rangle = G_{AB} = \bar{G}_{BA} \tag{A9}$$

forms a metric for functions on the shell. (Although a priori this matrix appears to be complex valued, it is actually real-symmetric and sparse, cf. Refs.[11, 12]. For now it suffices to follow Misner in denoting it as generically Hermitian.) The inverse to this metric G^{AB} can be used to raise indices on functions defined on the sphere.

Making use of this new metric, and with some further analysis, the approximation for the spherical harmonic coefficients

$$\Phi_{lm}(t,R) = \sum_{x\in\Gamma} \bar{R}_{lm}(x;R)w_x\Phi(t,x) \tag{A10}$$

follows with

$$R_{lm}(r;R) = \sum_{n=0}^{N} \bar{R}_n(R)Y^{nlm}(r,\theta,\phi) \tag{A11}$$

in terms of $Y^A = G^{BA}Y_B$, not Y_A.

Note that one need only store the combination $w_x\bar{R}_{lm}$ at points where $w_x \neq 0$ in order to compute the spherical harmonic components. This buries all the details of the computation in a relatively small table of numbers, and, since these numbers are not time dependent, this calculation need be done only once per simulation.

APPENDIX B: TEUKOLSKY WAVE SOLUTION

The general form of the spacetime metric for the Teukolsky wave solution [13] is

$$\begin{aligned} ds^2 &= -dt^2 + (1 + Af_{rr})dr^2 \\ &\quad + 2Bf_{r\theta}rdrd\theta + 2Bf_{r\phi}r\sin\theta drd\phi \\ &\quad + \left(1 + Cf^{(1)}_{\theta\theta} + Af^{(2)}_{\theta\theta}\right) r^2 d\theta^2 \\ &\quad + 2(A - 2C)f_{\theta\phi}r^2\sin\theta d\theta d\phi \\ &\quad + \left(1 + Cf^{(1)}_{\phi\phi} + Af^{(2)}_{\phi\phi}\right) r^2\sin^2\theta d\phi^2 \end{aligned} \tag{B1}$$

given in terms of the functions Eq. 5. The angular function are

$$f_{rr} = 2 - 3\sin^2\theta \tag{B2a}$$
$$f_{r\theta} = -3\sin\theta\cos\theta \tag{B2b}$$
$$f_{r\phi} = 0 \tag{B2c}$$
$$f^{(1)}_{\theta\theta} = 3\sin^2\theta \tag{B2d}$$
$$f^{(2)}_{\theta\theta} = -1 \tag{B2e}$$
$$f_{\theta\phi} = 0 \tag{B2f}$$
$$f^{(1)}_{\phi\phi} = -f^{(1)}_{\theta\theta} \tag{B2g}$$
$$f^{(2)}_{\phi\phi} = 3\sin^2\theta - 1 \tag{B2h}$$

for the $l = 2$, $m = 0$ case.

The Weyl scalar Ψ_4 for this spacetime is computed from the definition Eq. 2 using the Kinnersley tetrad, Eq. 8, and noting that, of the twelve non-zero components of the Riemann tensor associated with the metric Eq. B1, only

$$R_{t\theta t\theta} = -\frac{3}{2}r^2\sin^2\theta\frac{\partial^2 C}{\partial t^2} + \frac{1}{2}r^2\frac{\partial^2 A}{\partial t^2} \tag{B3a}$$
$$R_{t\phi t\phi} = \frac{3}{2}r^2\sin^4\theta\left(\frac{\partial^2 C}{\partial t^2} - \frac{\partial^2 A}{\partial t^2}\right) + \frac{1}{2}r^2\sin^2\theta\frac{\partial^2 A}{\partial t^2} \tag{B3b}$$
$$R_{t\theta r\theta} = -\frac{1}{8}r^3\sin^2\theta\left(3\frac{\partial^3 B}{\partial t^3} + \frac{\partial^3 A}{\partial t^3}\right) \tag{B3c}$$
$$R_{r\phi r\phi} = -\sin^2\theta R_{t\theta t\theta} \tag{B3d}$$
$$R_{r\theta r\theta} = -\frac{1}{\sin^2\theta}R_{t\phi t\phi} \tag{B3e}$$
$$R_{t\phi r\phi} = -\sin^2\theta R_{t\theta r\theta} \tag{B3f}$$

contribute to the sum.

[1] C. W. Misner, Class. Quant. Grav. **21**, S243 (2004).
[2] P. MacNeice, K. Olson, C. Mobarry, R. de Fainchtein, and C. Packer, Comput. Phys. Comm. **126**, 330 (2000).
[3] M. Alcubierre, G. Allen, C. Bona, D. Fiske, T. Goodale, F. S. Guzmán, I. Hawke, S. H. Hawley, S. Husa, M. Koppitz, et al., Class. Quant. Grav. **21**, 589 (2004).
[4] M. Shibata and T. Nakamura, Phys. Rev. D **52**, 5428 (1995).
[5] T. W. Baumgarte and S. L. Shapiro, Phys. Rev. D **59**, 024007 (1999), gr-qc/9810065.
[6] B. Imbiriba, J. Baker, D.-I. Choi, J. Centrella, D. R. Fiske, J. D. Brown, J. van Meter, and K. Olson, Phys. Rev. D **70**, 124025 (2004), gr-qc/0403048.
[7] S. A. Teukolsky, Phys. Rev. D **61**, 087501 (2000), gr-qc/9909026.
[8] D.-I. Choi, J. D. Brown, B. Imbiriba, J. Centrella, and P. MacNeice, J. Comp. Phys. **193**, 398 (2004).
[9] S. Chandrasekhar, *The Mathematical Theory of Black Holes* (Oxford University Press, 1992).
[10] J. Baker, M. Campanelli, and C. O. Lousto, Phys. Rev. D **65**, 044001 (2002).
[11] D. R. Fiske, Ph.D. thesis, University of Maryland, College Park (2004), http://hdl.handle.net/1903/1805.
[12] D. R. Fiske (2004), gr-qc/0412047.
[13] S. A. Teukolsky, Phys. Rev. D **26**, 745 (1982).
[14] W. Kinnersley, J. Math. Phys. **10**, 1195 (1969).
[15] B. Brügmann, Phys. Rev. D **54**, 7361 (1996).
[16] D. Brill and R. Lindquist, Phys. Rev. **131**, 471 (1963).
[17] D. Shoemaker, K. Smith, U. Sperhake, P. Laguna, E. Schnetter, and D. Fiske, Class. Quant. Grav. **20**, 3729 (2003), gr-qc/0301111.
[18] M. Alcubierre, B. Brügmann, P. Diener, M. Koppitz, D. Pollney, E. Seidel, and R. Takahashi, Phys. Rev. D **67**, 084023 (2003).